Inorg. Chem. **2005**, *44*, 1752–1762

Spectroscopic and Computational Studies on the Trans-μ-1,2-Peroxo-Bridged Dinickel(II) Species $[\{Ni(tmc)\}_2(O_2)](OTf)_2$: Nature of End-On Peroxo–Nickel(II) Bonding and Comparison with Peroxo–Copper(II) Bonding

Ralph Schenker,[†] Matthew T. Kieber-Emmons,[‡] Charles G. Riordan,[‡] and Thomas C. Brunold*[,†]

Department of Chemistry, University of Wisconsin—Madison, Madison, Wisconsin 53706, and Department of Chemistry and Biochemistry, University of Delaware, Newark, Delaware 19716

Received October 9, 2004

Resonance Raman (rR) spectroscopic and density functional theory (DFT) computational studies on a trans-μ-1,2-peroxo-bridged $(Ni^{2+})_2$ complex, $[\{(tmc)Ni^{2+}\}_2(O_2)]^{2+}$ (**1**, tmc = 1,4,8,11-tetramethyl-1,4,8,11-tetraazacyclotetradecane), are presented and discussed. These studies afford a detailed description of the geometric and electronic structures of the Ni_2O_2 core in **1** and provide a suitable basis for a quantitative comparison between Ni–peroxo and Cu–peroxo bonding. From a normal coordinate analysis of rR data of **1**, values of $k_{Ni-O} = 1.52$ mdyn/Å and $k_{O-O} = 2.58$ mdyn/Å are obtained for the Ni–O and O–O stretch force constants, respectively, which are considerably smaller than $k_{Cu-O} = 2.05$ mdyn/Å and $k_{O-O} = 3.09$ mdyn/Å reported for a representative trans-μ-1,2-peroxo-bridged $(Cu^{2+})_2$ complex, $[\{(TMPA)Cu^{2+}\}_2(O_2)]^{2+}$. These differences primarily reflect a strongly reduced covalency of the metal–peroxo bonds in **1** relative to the $(Cu^{2+})_2$ dimer as a result of the lower effective nuclear charge of Ni^{2+} than Cu^{2+}. DFT computations aimed at elucidating the reaction coordinate for the thermal decay of **1** reveal that the conversion of this species to a side-on peroxo $(Ni^{2+})_2$ dimer is electronically feasible but energetically unfavorable by ~85 kcal/mol due to the steric constraints imposed by the tmc supporting ligands. These results suggest that the decay of **1** to the crystallographically characterized final product, $[(tmc)Ni^{2+}OH]OTf$, proceeds without initial end-on → side-on peroxo $(Ni^{2+})_2$ core conversion.

Introduction

Nickel−dioxygen intermediates obtained by the reaction of low-valent Ni complexes with O_2 and H_2O_2 play a role in several stoichiometric and catalytic reactions. For example, Ni^{2+} azamacrocycles react with O_2 to yield putative Ni/O_2 intermediates capable of H-atom abstraction.[1] Also, bis-μ-oxo[2−4] and bis-μ-1,2-superoxo[4] bridged $(Ni^{3+})_2$ dimers have been shown to be competent of carrying out diverse organic functionalizations through intra- or intermolecular H-atom abstraction. Thus, nickel−dioxygen species possess significant potential for use as oxidation catalysts. Consequently, the development of a detailed understanding of the reaction mechanisms by which Ni/O_2 intermediates are formed and the factors influencing their reactivities is of great fundamental and practical interest.

Much emphasis in this respect has been placed on the related Cu/O_2 chemistry, from which a common mechanism for O_2 activation by copper complexes has emerged.[5] Typically, a Cu^+ precursor equipped with a nitrogen supporting ligand reacts with dioxygen to form a monomeric

* Author to whom correspondence should be addressed. E-mail: brunold@chem.wisc.edu.

[†] University of Wisconsin—Madison.

[‡] University of Delaware.

(1) (a) Kimura, E.; Sakonaka, A.; Machida, R. *J. Am. Chem. Soc.* **1982**, *104*, 4255−4257. (b) Kimura, E.; Machida, R. *J. Chem. Soc., Chem. Commun.* **1984**, 499−500. (c) Kushi, Y.; Machida, R.; Kimura, E. *J. Chem. Soc., Chem. Commun.* **1985**, 216−218. (d) Chen, D.; Martell, A. E. *J. Am. Chem. Soc.* **1990**, *112*, 9411−9412. (e) Cheng, C.-C.; Gulia, J.; Rokita, S. E.; Burrows, C. J. *J. Mol. Catal. A* **1996**, *113*, 379−391. (f) Berkessel, A.; Bats, J. W.; Schwarz, C. *Angew. Chem., Int. Ed. Engl.* **1990**, *29*, 106−108.

(2) (a) Hikichi, S.; Yoshizawa, M.; Sasakura, Y.; Akita, M.; Moro-oka, Y. *J. Am. Chem. Soc.* **1998**, *120*, 10567−10568. (b) Hikichi, S.; Yoshizawa, M.; Sasakura, Y.; Komatsuzaki, H.; Moro-oka, Y.; Akita, M. *Chem.—Eur. J.* **2001**, *7*, 5012−5028.

(3) Itoh, S.; Bandoh, H.; Nakagawa, M.; Nagamoto, S.; Kitagawa, T.; Karlin, K. D.; Fukuzumi, S. *J. Am. Chem. Soc.* **2001**, *123*, 11168−11178.

(4) Shiren, K.; Ogo, S.; Fujinami, S.; Hayashi, H.; Suzuki, M.; Uehara, A.; Watanabe, Y.; Moro-oka, Y. *J. Am. Chem. Soc.* **2000**, *122*, 254−262.

10.1021/ic048584j CCC: $30.25
Published on Web 02/17/2005

Cu species possessing a side-on bound O_2 moiety, which then reacts with a second molecule of the Cu^+ precursor to form a binuclear complex.[5,6] Dimers with bi- or tridentate N-donor ligands adopt μ-η^2:η^2-peroxo (side-on) $(Cu^{2+})_2$ or bis-μ-oxo $(Cu^{3+})_2$ cores[5,7] that often coexist in an equilibrium,[8] whereas species with tetradentate ligands favor a trans-μ-1,2-peroxo (end-on) $(Cu^{2+})_2$ core.[5b,6,9−11] While the majority of bis-μ-oxo $(Ni^{3+})_2$ dimers reported to date have been generated by reacting the corresponding bis-μ-hydroxo-bridged $(Ni^{2+})_2$ complexes with H_2O_2,[2,3,4] we recently discovered that [(PhTt^{tBu})Ni$^+$CO], where (PhTt^{tBu}) is a tridentate thioether ligand, is capable of activating O_2 to yield the bis-μ-oxo dimer [{(PhTt^{tBu})Ni^{3+}}$_2$(μ-O)$_2$].[12,13] We hypothesized that the mechanism of O_2 activation by Ni^+ species would be similar to that established for copper systems (vide supra); the presumed key steps in this process are summarized in Scheme 1.

To assess the viability of this hypothesis, we sought to prevent dimerization by replacing the *tert*-butyl substituent

Scheme 1

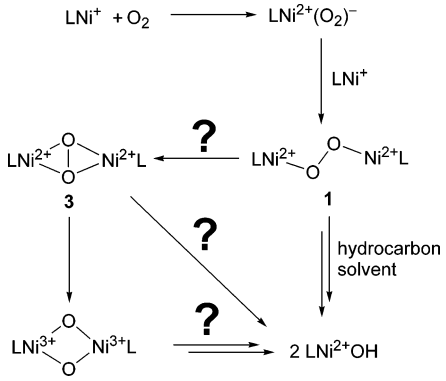

of (PhTt^{tBu}) with the sterically more demanding 1-adamantyl group. Indeed, reaction of [(PhTt^{Ad})Ni$^+$CO] with O_2 yielded a monomeric side-on superoxo Ni^{2+} complex, [(PhTt^{Ad})-Ni^{2+}O$_2$], that could be trapped and studied spectroscopically.[14] Interestingly, this species reacts with [(PhTt^{tBu})-Ni$^+$CO] to yield the asymmetric bis-μ-oxo dimer [(PhTt^{Ad})-Ni^{3+}(μ-O)$_2$Ni^{3+}(PhTt^{tBu})], thus demonstrating that a side-on superoxo Ni^{2+} species may indeed serve as an intermediate in the mechanism of O_2 activation by Ni^+ complexes (Scheme 1).[14] Whether a μ-η^2:η^2-peroxo-bridged $(Ni^{2+})_2$ species plays a role in this mechanism remains uncertain at present. While the transient formation of such species has been invoked in the conversion of bis-μ-hydroxo $(Ni^{2+})_2$ complexes to their bis-μ-oxo $(Ni^{3+})_2$ derivatives on the basis of kinetic studies,[3] no direct experimental evidence for its existence is available currently. Recent density functional theory (DFT) computations on a hypothetical side-on peroxo-bridged $(Ni^{2+})_2$ complex, [{(PhTt^{tBu})Ni^{2+}}$_2$(μ-η^2:η^2-O)$_2$], revealed that its conversion to the well-characterized bis-μ-oxo isomer, [{(PhTt^{tBu})Ni^{3+}}$_2$(μ-O)$_2$], occurs essentially barrierless and with a large driving force of $\Delta H = 32$ kcal/mol,[13] thus providing a rationale for the experimental difficulty of stabilizing a μ-η^2:η^2-peroxo-bridged $(Ni^{2+})_2$ species.

In an attempt to render access to a side-on peroxo coordination more difficult and hence to increase the likelihood of observing an end-on peroxo-bridged Ni_2 species, we employed a tetradentate macrocycle that coordinates Ni in a planar fashion. Following this approach, we discovered that the reaction of [(tmc)Ni$^+$]OTf (tmc = 1,4,8,-11-tetramethyl-1,4,8,11-tetraazacyclotetradecane) with O_2 at low temperature yields [{(tmc)Ni^{2+}}$_2$(O$_2$)]$^{2+}$ (**1**), which is the only trans-μ-1,2-peroxo-bridged Ni_2 dimer characterized to date.[15] This thermally unstable species ($\tau_{1/2} \approx 4$ min at −45 °C) reacts via an as yet ill-defined, brown intermediate ($\tau_{1/2} \approx 4$ h at −40 °C)[16] to yield the monomeric final product [(tmc)Ni^{2+}OH]OTf (Scheme 1), in which the hydrogen atom of the OH$^-$ ligand originates from the acetonitrile solvent.[15]

A plausible mechanistic scenario for the decay of **1** to [(tmc)Ni^{2+}OH]OTf involves initial isomerization of **1** to its side-on peroxo derivative, followed by O−O bond cleavage

(5) For recent reviews, see: (a) Que, L., Jr.; Tolman, W. B. *Angew. Chem., Int. Ed.* **2002**, *41*, 1114−1137. (b) Mirica, L. M.; Ottenwaelder, X.; Stack, T. D. P. *Chem. Rev.* **2004**, *104*, 1013−1045.
(6) Zhang, C. X.; Kaderli, S.; Costas, M.; Kim., E.-I.; Neuhold, Y.-M.; Karlin, K. D.; Zuberbühler, A. D. *Inorg. Chem.* **2003**, *42*, 1807−1824.
(7) (a) Kitajima, N.; Fujisawa, K.; Moro-oka, Y.; Toriumi, K. *J. Am. Chem. Soc.* **1989**, *111*, 8975−8976. (b) Mahapatra, S.; Halfen, J. A.; Wilkinson, E. C.; Pan, G.; Cramer, C. J.; Que, L., Jr.; Tolman, W. B. *J. Am. Chem. Soc.* **1995**, *117*, 8865−8866. (c) Halfen, J. A.; Mahapatra, S.; Wilkinson, E. C.; Kaderli, S.; Young, V. G., Jr.; Que, L., Jr.; Zuberbühler, A. D.; Tolman, W. B. *Science* **1996**, *271*, 1397−1400. (d) Tolman, W. B. *Acc. Chem. Res.* **1997**, *30*, 227−237. (e) Mahapatra, S.; Young, V. G., Jr.; Tolman, W. B. *Angew. Chem., Int. Ed. Engl.* **1997**, *36*, 130−133. (f) Mahadevan, V.; Hou, Z.; Cole, A. P.; Root, D. E.; Lal, T. K.; Solomon, E. I.; Stack, T. D. P. *J. Am. Chem. Soc.* **1997**, *119*, 11996−11997. (g) Enomoto, M.; Aida, T. *J. Am. Chem. Soc.* **1999**, *121*, 874−875. (h) Mahadevan, V.; DuBois, J. L.; Hedman, B.; Hodgson, K. O.; Stack, T. D. P. *J. Am. Chem. Soc.* **1999**, *121*, 5583−5584. (i) Straub, B. F.; Rominger, F.; Hofmann, P. *Chem. Commun.* **2000**, 1611−1612. (j) Funahashi, Y.; Nakaya, K.; Hirota, S.; Yamauchi, O. *Chem. Lett.* **2000**, 1172. (k) Spencer, D. J. E.; Aboelella, N. W.; Reynolds, A. M.; Holland, P. L.; Tolman, W. B. *J. Am. Chem. Soc.* **2002**, *124*, 2108−2109.
(8) (a) Mahapatra, S.; Kaderli, S.; Llobet, A.; Neuhold, Y.-M.; Palanché, T.; Halfen, J. A.; Young, V. G., Jr.; Kaden, T. A.; Que, L., Jr.; Zuberbühler, A. D.; Tolman, W. B. *Inorg. Chem.* **1997**, *36*, 6343−6356. (b) Itoh, S.; Taki, M.; Nakao, H.; Holland, P. L.; Tolman, W. B.; Que, L., Jr.; Fukuzumi, S. *Angew. Chem., Int. Ed.* **2000**, *39*, 398−400. (c) Obias, H. V.; Lin, Y.; Murthy, N. N.; Pidcock, E.; Solomon, E. I.; Ralle, M.; Blackburn, N. J.; Neubold, Y. M.; Zuberbühler, A. D.; Karlin, K. D. *J. Am. Chem. Soc.* **1998**, *120*, 12960−12961. (d) Pidcock, E.; DeBeer, S.; Obias, H. V.; Hedman, B.; Hodgson, K. O.; Karlin, K. D.; Solomon, E. I. *J. Am. Chem. Soc.* **1999**, *121*, 1870−1878. (e) Cahoy, J.; Holland, P. L.; Tolman, W. B. *Inorg. Chem.* **1999**, *38*, 2161−2168. (f) Hayashi, H.; Fujinami, S.; Nagamoto, S.; Ogo, S.; Suzuki, M.; Uehara, A.; Watanabe, Y.; Kitagawa, T. *J. Am. Chem. Soc.* **2000**, *122*, 2124−2125. (g) Mahadevan, V.; Henson, M.; Solomon, E. I.; Stack, T. D. P. *J. Am. Chem. Soc.* **2000**, *122*, 10249−10250. (h) Henson, M. J.; Mukherjee, P.; Root, D. E.; Stack, T. D. P.; Solomon, E. I. *J. Am. Chem. Soc.* **1999**, *121*, 10332−10345.
(9) (a) Jacobson, R. R.; Tyeklár, Z.; Karlin, K. D.; Liu, S.; Zubieta, J. *J. Am. Chem. Soc.* **1988**, *110*, 3690−3692. (b) Tyeklár, Z.; Jacobson, R. R.; Wei, N.; Murthy, N. N.; Zubieta, J.; Karlin, K. D. *J. Am. Chem. Soc.* **199**3, *11*5, 2677−2689.
(10) Halfen, J. A.; Young, J., V. G.; Tolman, W. B. *J. Am. Chem. Soc.* **1996**, *118*, 10920−10921.
(11) Weitzer, M.; Schindler, S.; Brehm, G.; Schneider, S.; Hörmann, E.; Jung, B.; Kaderli, S.; Zuberbühler, A. D. *Inorg. Chem.* **2003**, *42*, 1800−1806.
(12) Mandimutsira, B. S.; Yamarik, J. L.; Brunold, T. C.; Gu, W.; Cramer, S. P.; Riordan, C. G. *J. Am. Chem. Soc.* **2001**, *123*, 9194−9195.
(13) Schenker, R.; Mandimutsira, B. S.; Riordan, C. G.; Brunold, T. C. *J. Am. Chem. Soc.* **2002**, *124*, 13842−13855.
(14) Fujita, K.; Schenker, R.; Gu, W.; Brunold, T. C.; Cramer, S. P.; Riordan, C. G. *Inorg. Chem.* **2004**, *43*, 3324−3326.
(15) Kieber-Emmons, M. T.; Schenker, R.; Yap, G. P. A.; Brunold, T. C.; Riordan, C. G. *Angew. Chem.* **2004**, *43*, 6716−6718.
(16) Kieber-Emmons, M. T.; Riordan, C. G. Unpublished results.

to yield a bis-μ-oxo $(Ni^{3+})_2$ species that then decays to the final hydroxo complex by H-atom abstraction from the solvent. To adopt a side-on peroxo $(Ni^{2+})_2$ core, the tmc ligand in **1** would have to rearrange such as to change its coordination to the Ni center from planar to facial, an arrangement previously observed for tetraaza macrocycles.[17] A reaction path in which an end-on peroxo species converts to its side-on peroxo derivative would not be unprecedented. For instance, such a conversion has been implicated in the process of O_2 binding to the $(Cu^{+})_2$ site of deoxyhemocyanin based on a DFT study.[18] Further, reduced (diferrous) methane monooxygenase reacts with O_2 to yield a μ-1,2-peroxo-bridged $(Fe^{3+})_2$ species that has been proposed to convert to the putative bis-μ-oxo $(Fe^{4+})_2$ key reactive intermediate (compound Q) via transient formation of a μ-η^2:η^2-peroxo $(Fe^{3+})_2$ dimer.[19] The end-on → side-on peroxo core conversion has also been observed, and studied kinetically, for $[(N4)(Cu^{2+})_2(O)_2]$;[20] however, in this case the conversion presumably occurs via transient formation of a dimeric $(Cu^{2+})_2$−peroxo species in which the O_2 moiety is terminally bound to a single copper.[21]

An important step toward the development of a molecular-level understanding of the reactivity of **1** involves elucidating the geometric and electronic structures of the corresponding Ni_2O_2 core on a quantitative level. While several spectroscopic and theoretical studies performed by Solomon and co-workers[22,23] as well as Comba, Karlin, and co-workers[24] have provided detailed insight into metal−peroxo and O−O bonding in μ-1,2-peroxo-bridged $(Cu^{2+})_2$ and $(Fe^{3+})_2$ dimers, the nature of Ni−O and O−O bonding in μ-1,2-peroxo-bridged $(Ni^{2+})_2$ complexes is presently unexplored. Here, we present detailed spectroscopic and computational studies on the trans-μ-1,2-peroxo-bridged dimer **1** to fill this gap. The force constants of the metal−peroxo and intraperoxo stretching vibrations of the Ni_2O_2 core in **1** are determined from a normal coordinate analysis (NCA) of our resonance Raman (rR) data and compared to those reported for the Cu_2O_2 core of the crystallographically characterized[9] trans-μ-1,2-peroxo-bridged dimer $[\{(TMPA)Cu^{2+}\}_2(O_2)]^{2+}$ (**2**, TMPA = tris-(2-pyridylmethyl)amine).[22] DFT electronic structure calculations are employed to develop a quantitative bonding description for **1** and to obtain insight into the factors that influence the Ni−O and O−O bond strengths in μ-1,2-peroxo-bridged $(Ni^{2+})_2$ dimers. To assess the feasibility of a mechanistic pathway for the decay of **1** to $[(tmc)Ni^{2+}OH]$-OTf involving a μ-η^2:η^2-peroxo-bridged $(Ni^{2+})_2$ species, additional computations are presented for the hypothetical complex $[\{(tmc)Ni^{2+}\}_2(\mu\text{-}\eta^2\text{:}\eta^2\text{-}O_2)]^{2+}$ (**3**), and the reaction coordinate and energy barrier for the interconversion between **1** and **3** are evaluated.

Experimental Methods

Spectroscopy. Samples of the trans-μ-1,2-peroxo-bridged $(Ni^{2+})_2$ dimer $[\{(tmc)Ni^{2+}\}_2(O_2)]^{2+}$ (**1**) in THF solution were prepared as described previously.[15] Absorption spectra of **1** in THF were recorded at 195 K using a Cary 50 spectrometer (Varian). Isotopically pure samples of **1** for rR experiments were prepared in NMR tubes by exposure of ~5 mM solutions of *RRSS*-[(tmc)-Ni^{+}]OTf in THF to either $^{16}O_2$ or $^{18}O_2$ at 196 K. rR spectra were recorded upon excitation with Ar^{+} (Coherent I-305) or Kr^{+} (Coherent I-302) ion lasers with an incident laser power of 20 mW (10 mW for excitation profile data) at the sample. The scattered light was collected at an ~135° backscattering angle from the surface of the sample, which was kept in an NMR tube that was immersed in an EPR dewar filled with liquid N_2. The scattered light was dispersed by a triple monochromator (Acton Research) using either 1200 or 2400 grooves/mm gratings and detected by a back-illuminated CCD camera (Princeton Instruments, 1340 × 100 pixels). Raman shifts and intensities were calibrated relative to the 880 cm^{-1} peak of the solvent THF.

Normal Coordinate Analysis. A normal coordinate analysis (NCA) of the vibrational data of **1** was performed by assuming an idealized C_{2h} geometry of the Ni_2O_2 core with Ni−O and O−O bond lengths of 2.015 and 1.436 Å, respectively, and a Ni−O−O bond angle of 120°, as derived from the DFT geometry-optimized model of **1** (vide infra). This analysis was based on the Wilson FG matrix method using a Urey−Bradley force field as implemented in a modified version of the Schachtschneider program.[25]

Electronic Structure Calculations. DFT computations were performed on a cluster composed of 20 Intel Xeon 2.4 GHz processors (Ace Computers) using the Amsterdam Density Functional (ADF) 2003.01 software package.[26] A trans-μ-1,2-peroxo Ni_2O_2 core conformation was assumed in generating the initial computational model of **1**, since the corresponding cis conformation is expected to be considerably less stable on the basis of steric considerations (note that, as a general rule, μ-1,2 peroxo dimers only adopt the cis conformation if the two metal centers are linked by additional bridging ligands). The conformation of the tmc macrocycle was based on the crystallographically characterized *RRSS*-isomer of $[(tmc)Ni^{+}]OTf{\cdot}NaOTf$,[27] the starting material used to generate **1**, where the methyl groups were replaced by protons. Additional computations were performed on (i) a sterically unconstrained derivative of **1** in which tmc was replaced by four ammine groups, $[\{(NH_3)_4Ni^{2+}\}_2(O_2)]^{2+}$ (model **1′**), (ii) a hypothetical side-on peroxo derivative of **1′** (model **3′**), and (iii) another hypothetical side-on peroxo derivative of **1**, $[\{(tmc)Ni^{2+}\}_2(O)_2]^{2+}$ (model **3***), possessing the complete tmc ligand (i.e., including the methyl groups) in a "folded" conformation as observed for the crystallo-

(17) (a) Cabbiness, D. K.; Margerum, D. W. *J. Am. Chem. Soc.* **1970**, *92*, 2151−2153. (b) Ito, H.; Ito, T. *Bull. Chem. Soc. Jpn.* **1985**, *58*, 1755−1760. (c) Ito, H.; Ito, T. *Acta Crystallogr., Sect. C* **1985**, *41*, 1598−1602. (d) Lu, T.-H.; Shui, W.-Z.; Tung, S.-F.; Chi, T.-Y.; Liao, F.-L.; Chung, C.-S. *Acta Crystallogr., Sect. C* **1998**, *54*, 1071−1072.

(18) Metz, M.; Solomon, E. I. *J. Am. Chem. Soc.* **2001**, *123*, 4938−4950.

(19) Valentine, A. M.; Stahl, S. S.; Lippard, S. J. *J. Am. Chem. Soc.* **1999**, *121*, 3876−3887.

(20) N4 represents a hydrocarbon-linked bis(2-(2-pyridyl)ethyl)amine.

(21) Jung, B.; Karlin, K. D.; Zuberbühler, A. D. *J. Am. Chem. Soc.* **1996**, *118*, 3763−3764.

(22) Baldwin, M. J.; Ross, P. K.; Pate, J. E.; Tyeklár, Z.; Karlin, K. D.; Solomon, E. I. *J. Am. Chem. Soc.* **1991**, *113*, 8671−8679.

(23) Brunold, T. C.; Tamura, N.; Kitajima, N.; Moro-oka, Y.; Solomon, E. I. *J. Am. Chem. Soc.* **1998**, *120*, 5674−5690.

(24) Comba, P.; Hilfenhaus, P.; Karlin, K. D. *Inorg. Chem.* **1997**, *36*, 2309−2313.

(25) (a) Schachtschneider, J. H. *Technical Report No. 57-65*; Shell Development Co.: Emeryville, CA, 1966. (b) Fuhrer, H.; Kartha, V. B.; Kidd, K. G.; Krueger, P. J.; Mantsch, H. H. *Computer Programs for Infrared Spectroscopy*; Bulletin No. 15; National Research Council of Canada: Ottawa, Canada, 1976.

(26) (a) Baerends, E. J.; Ellis, D. E.; Ros, P. *Chem. Phys.* **1973**, *2*, 41−51. (b) te Velde, G.; Baerends, E. J. *Int. J. Comput. Phys.* **1992**, *99*, 84−98.

(27) Ram, M. S.; Riordan, C. G.; Ostrander, R.; Rheingold, A. L. *Inorg. Chem.* **1995**, *34*, 5884−5892.

graphically characterized species $[Ni_3(tmc)_3(CO_3)_2(OTf)_2]$[16] and $[Co^{2+}(tmc)(PhenSQ)]PF_6$.[28] As described in the Discussion, during geometry optimization **3*** converted spontaneously to a trans-μ-1,2-peroxo Ni_2O_2 dimer (**1a***) while the folded tmc conformation was preserved. To evaluate the energetic penalty associated with tmc folding in the latter species, an additional model of **1** was generated possessing the full tmc macrocycle, like **1a***, but in an unfolded conformation (model **1***). For all models, refined atomic coordinates (provided in Tables S1−S8, Supporting Information) were obtained through DFT energy minimization using the algorithm of Versluis and Ziegler.[29] All computations were carried out using an integration constant of 4.0, the Vosko−Wilk−Nusair local density approximation[30] for the exchange and correlation energies, and the nonlocal gradient corrections of Becke[31] and Perdew.[32] A triple-ζ Slater-type orbital (STO) basis set with a single-ζ STO polarization function (ADF basis set IV) was used for all atoms. Core orbitals were frozen through 1s (C, N, O) and 2p (Ni).

To explore the magnetic properties and develop a quantitative bonding description of **1**, single-point hybrid DFT calculations were performed on the geometry-optimized models of **1** described above using the ORCA 2.2.94 software package developed by Dr. Frank Neese.[33] Becke's three-parameter hybrid functional[34] for exchange together with the Lee−Yang−Parr correlation functional (B3LYP/G) was employed.[35] A triple-ζ Gaussian-type orbital (GTO) basis (Ahlrich's TZV)[36] was chosen with three, two, and one polarization functions for the Ni, O, and N atoms, respectively,[37] while the remaining atoms were modeled with the SV(P) (Ahlrich's polarized split valence) basis.[36] The SV/C auxiliary basis set was used for all atoms,[38] and an integration grid of size 4 (Lebedev 302 points) was employed in all calculations.

Vertical excitation energies and transition dipole moments were calculated by the time-dependent DFT (TD-DFT) method[39] within the Tamm−Dancoff approximation[40] as implemented in ORCA, employing the same functionals and basis sets as described above for the single-point calculations. Convergence of the TD-DFT calculations required the use of the resolution of the identity approximation in calculating the Coulomb term.[41] A total of 50 excited states were calculated by including all one-electron excitations within an energy window of ±3 hartrees with respect to the HOMO/LUMO energies. Isosurface plots of molecular orbitals (MOs) as well as of electron density difference maps (EDDMs) and the total unpaired spin density distribution obtained from the spin-unrestricted ORCA calculations were generated with the gOpenMol software developed by Leif Laaksonen (using isodensity values of 0.05, 0.005, and 0.01 au, respectively).[42]

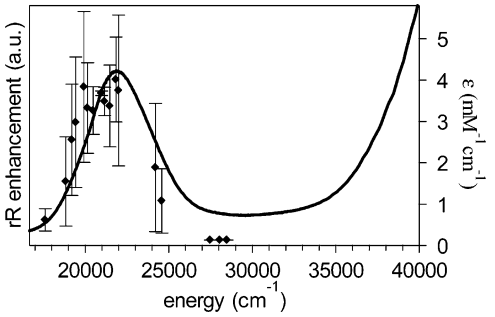

Figure 1. 195 K electronic absorption spectrum (solid line) of **1** in THF, superimposed by the rR excitation profile (full diamonds) of the dominant vibrational feature observed at 778 cm^{-1}. The profile shows the average of 3 data sets; the error bars indicate the corresponding standard deviation.

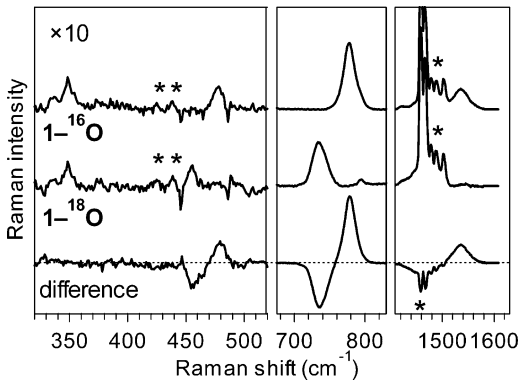

Figure 2. 77 K rR spectra for 502 nm excitation of **1** prepared with $^{16}O_2$ (top) and $^{18}O_2$ (middle) and difference thereof (bottom). Note that the low-frequency portions of the spectra are scaled by a factor of 10. Solvent peaks are marked with an asterisk.

Results and Analysis

A. Spectroscopy. The 195 K solution absorption spectrum of **1** in THF exhibits a single, intense broad feature centered at 21 880 cm^{-1} in the spectral region below 35 000 cm^{-1} (Figure 1).[43] To identify the nature of the corresponding transition, rR data were collected using various excitation wavelengths. The rR spectrum of **1** prepared with $^{16}O_2$ (**1-$^{16}O_2$**) excited at 502 nm (Figure 2) is dominated by an intense peak at 778 cm^{-1} that downshifts to 735 cm^{-1} for samples prepared with $^{18}O_2$ (**1-$^{18}O_2$**). An additional, much weaker feature at 479 cm^{-1} is observed for **1-$^{16}O_2$** that downshifts to 456 cm^{-1} in the spectrum of **1-$^{18}O_2$** (note that in Figure 2 different scales are used for the low-frequency and high-frequency regions). The isotopic shifts of −43 and −23 cm^{-1} of the 778/735 cm^{-1} and 479/456 cm^{-1} modes compare well with the values of −50 and −28 cm^{-1} calculated for diatomic

(28) Caneschi, A.; Dei, A.; Gatteschi, D.; Tangoulis, V. *Inorg. Chem.* **2002**, *41*, 3508−3512.
(29) Versluis, L.; Ziegler, T. *J. Chem. Phys.* **1988**, *88*, 322−329.
(30) Vosko, S. H.; Wilk, L.; Nusair, M. *Can. J. Phys.* **1980**, *58*, 1200−1211.
(31) Becke, A. D. *J. Chem. Phys.* **1986**, *84*, 4524−4529.
(32) Perdew, J. P. *Phys. Rev. B* **1986**, *33*, 8822−8824.
(33) Neese, F. Max Planck Institute for Bioinorganic Chemistry, D-45470 Mülheim/Ruhr, Germany; neese@mpi-muelheim.mpg.de.
(34) Becke, A. D. *J. Chem. Phys.* **1993**, *98*, 1372−1377. (b) Becke, A. D. *J. Chem. Phys.* **1993**, *98*, 5648−5652.
(35) Lee, C.; Yang, W.; Parr, R. G. *Phys. Rev. B* **1988**, *37*, 785−789.
(36) Schäfer, A.; Horn, H.; Ahlrichs, R. *J. Chem. Phys.* **1992**, *97*, 2571−2577.
(37) The Ahlrichs (2d, 2p, 2d2fg, and 3p2df) polarization functions were obtained from the TurboMole basis set library under ftp.chemie.uni-karlsruhe.de/pub/basen.
(38) The Ahlrichs auxiliary basis sets were obtained from the TurboMole basis set library under ftp.chemie.uni-karlsruhe.de/pub/cbasen. Weigend, F.; Häser, M. *Theor. Chem. Acc.* **1997**, *97*, 331−340.
(39) (a) Bauernschmitt, R.; Ahlrichs, R. *Chem. Phys. Lett.* **1996**, *256*, 454−464. (b) Casida, E. M.; Jamorski, C.; Casida, K. C.; Salahub, D. R. *J. Chem. Phys.* **1998**, *108*, 4439−4449. (c) Stratman, R. E.; Scuseria, G. E.; Frisch, M. J. *J. Chem. Phys.* **1998**, *109*, 8218−8224.
(40) (a) Hirata, S.; Head-Gordon, M. *Chem. Phys. Lett.* **1999**, *302*, 375−382. (b) Hirata, S.; Head-Gordon, M. *Chem. Phys. Lett.* **1999**, *314*, 291−299.
(41) Neese, F.; Olbrich, G. *Chem. Phys. Lett.* **2002**, *362*, 170−178.
(42) (a) Laaksonen, L. *J. Mol. Graphics* **1992**, *10*, 33−34. (b) Bergman, D. L.; Laaksonen, L.; Laaksonen, A. *J. Mol. Graphics Modell.* **1997**, *15*, 301−306.
(43) In ref 15 a value of $\lambda = 465$ nm ($\nu = 21\,505$ cm^{-1}) was reported for the peak position of this band in the 229 K solution absorption spectrum of **1** in acetonitrile. The slightly different position obtained here is due to the different temperature rather than the different solvent used in our study.

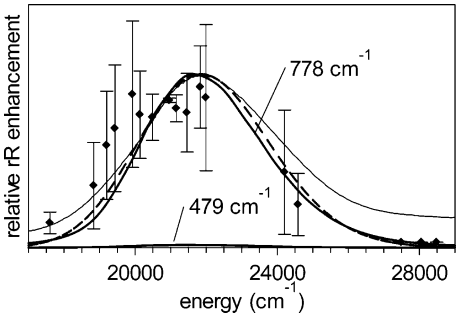

Figure 3. Simulated absorption spectrum (broken line) and rR excitation profile data (solid lines) using time-dependent Heller theory[45] with the dimensionless excited-state distortion parameters $|\Delta_{778}| = 2.45$ and $|\Delta_{479}| = 0.5$. The experimental absorption spectrum (thin solid line) and rR excitation profile data (symbols) are shown for comparison.

O−O and Ni−O harmonic oscillators, respectively. As similar values have also been reported for the trans-μ-1,2-peroxo-bridged $(Cu^{2+})_2$ dimer **2**,[22] it is relatively straightforward to assign the 778/735 cm^{-1} and 479/456 cm^{-1} modes to the totally symmetric O−O and Ni−O stretches, respectively. An additional isotope-sensitive feature of **1**-^{16}**O$_2$** is observed at 1536 cm^{-1} that downshifts to ~1455 cm^{-1} in **1**-^{18}**O$_2$**. The frequency and isotopic shift of this feature suggest that it corresponds to the first overtone of the O−O stretch. Finally, two isotope-insensitive bands can be discerned at 336 and 349 cm^{-1} that are tentatively assigned to Ni−N stretches.

As the dominant absorption band at 21880 cm^{-1} is closely mirrored by the rR excitation profile of the 778 cm^{-1} mode of **1**-^{16}**O$_2$** (Figure 1), this feature is assigned to a peroxo → Ni^{2+} CT transition.[44] To obtain further insight into the nature of the corresponding excited state, the rR excitation profile data in Figure 1 were analyzed within the framework of the time-dependent Heller theory.[45] The main objective of this analysis was to obtain the dimensionless displacement Δ_n of the excited state relative to the ground state along each normal coordinate n, as this information can be used to estimate excited-state distortions (see section D.3). Although the experimental rR excitation profile of the 479 cm^{-1} mode could not be determined independently due to the low intensity of this feature, it appears to parallel the profile of the intense 778 cm^{-1} mode. Therefore, a uniform intensity ratio of 0.015:1 was used in our Heller analysis for these two modes, as determined by Gaussian fits of the corresponding bands in the rR spectrum obtained with 502 nm excitation. As shown in Figure 3, with values of $|\Delta_{778}| = 2.45$ and $|\Delta_{479}| = 0.5$ the experimental absorption and rR excitation profile data of **1** are reasonably well reproduced by our simulations.

B. DFT Computations: Molecular Structure of 1. The thermal instability has thus far precluded crystallographic characterization of **1**; therefore, its molecular structure was explored through DFT geometry optimizations as described in Experimental Methods. Spin-unrestricted calculations were performed on both the high-spin (HS; $S = 2$) and the broken-symmetry (BS; $M_S = 0$) dimer ground states. The HS state with $S = 2$, $|M_S| = 2$ is the only spin state in this exchange-coupled dimer composed of two high-spin $S = 1$ Ni^{2+} centers that is well described by a single determinant, whereas the BS wave function contains contributions from the $M_S = 0$ components of all the dimer spin states (i.e., $S = 0$, 1, and 2). Nonetheless, because in the BS state the two Ni centers carry large amounts of oppositely signed unpaired spin density (±1.32; see Table S9), the corresponding wave function provides a reasonable description of the actual $S = 0$ ground state associated with two antiferromagnetically coupled $S = 1$ Ni^{2+} centers.

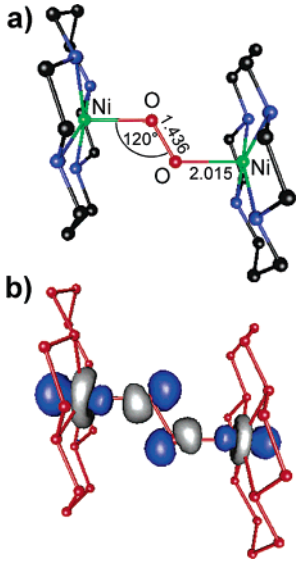

Figure 4. Energy-minimized structure of **1** (a) and isosurface plot of the singly occupied natural orbital that provides the dominant antiferromagnetic exchange pathway in **1** (b, isodensity value of 0.05 au), obtained from B3LYP DFT computation on the BS ($M_S = 0$) state.

The molecular structure of **1** as obtained from the geometry optimization in the BS state is shown in Figure 4a. The overall symmetry of the dimer complex is approximately C_2, with the rotation axis perpendicular to the plane defined by the Ni_2O_2 core. Each Ni is in a square-pyramidal ligand environment with a Ni−O bond length of 2.015 Å and an average Ni−N bond length of 2.101 Å. These values are similar to those found in [(tmc)Ni^{2+}OH]OTf[15] and are consistent with the high-spin d^8 electron configuration of Ni^{2+} in **1**. The O−O bond length of 1.436 Å is typical for a peroxo species, whereas the Ni−O−O bond angle of $\gamma = 120.0°$ is considerably larger than the Cu−O−O bond angle of 107.7° in **2**. The Ni−O−O−Ni core is relatively planar with a dihedral angle of $\tau = 8.5°$. To explore whether the omission of the methyl groups of the tmc ligand in the computational model could affect the DFT-optimized molecular structure of **1**, these methyl groups were reintroduced after geometry optimization, and the resulting complete model was examined using the Chem3D program in space-filling mode. No additional steric clash induced by the methyl substituents was found, suggesting that the tmc ligand truncation

(44) As the sample is very susceptible to photodecomposition upon laser excitation, this profile was obtained by averaging three independent data sets.

(45) (a) Heller, E. J. *Acc. Chem. Res.* **1981**, *14*, 368. (b) Zink, J. I.; Kim Shin, K.-S. In *Advances in Photochemistry*; Volman, D. H., Hammond, G. S., Neckers, D. C., Eds.; John Wiley: New York, 1991; Vol. 16, p 119. (c) Heller, E. J. *J. Chem. Phys.* **1975**, *62*, 1544.

had a minimal impact on the core geometry, including the Ni−O−O angle γ.

For the HS dimer state of **1**, Ni−O and O−O bond lengths of 2.034 and 1.401 Å, respectively, were obtained. Interestingly, γ increased to 125.8° while the Ni−O−O−Ni core became significantly less planar ($\tau = 15.7°$) than in the BS state. To explore the source of this pronounced difference in τ between the HS and BS states as well as the influence of the steric constraints imposed by the tmc ligand on γ, computations were also performed on a simplified model of **1**, $[\{(NH_3)_4Ni^{2+}\}_2(O_2)]^{2+}$ (**1′**), for both the HS ($S = 2$) and the BS ($M_S = 0$) dimer states. Interestingly, while for the HS states of **1′** and **1** the optimized dihedral angles are nearly identical ($\tau = 16.1$ and 15.7°, respectively), for the BS states they differ substantially ($\tau = 0$ and 8.5°, respectively), indicating a considerably more planar core in **1′** than in **1** (Table S9). Furthermore, for both states, γ decreased by ∼11° upon replacement of the tmc ligand of **1** by ammines to generate the sterically less constrained model **1′**. Together, these results suggest that the nonplanarity of the Ni_2O_2 core in **1** has both electronic and steric origins, whereas the relatively large Ni−O−O angle is primarily a consequence of the steric constraints imposed by the rigid tmc ligands on the two monomer halves.

C. Ground-State Properties. 1. Normal Coordinate Analysis. To determine the Ni−O and O−O bond strengths and to obtain the eigenvectors of the normal modes associated with the Ni_2O_2 core, a normal coordinate analysis (NCA) was performed of the rR data of **1**. Inspection of the rR spectra in Figure 2 reveals that contributions from Ni−N stretching modes are minor, and the magnitudes of the observed $^{16}O_2 \rightarrow {}^{18}O_2$ isotopic shifts for both the Ni−O and O−O stretches are close to the corresponding values predicted for isolated harmonic oscillators (section A). Therefore, it is reasonable to limit the NCA to the four atoms of the Ni_2O_2 core, allowing us to use a Urey−Bradley force field identical with that employed by Baldwin et al. in their analysis of the core vibrations of **2**.[22] The $N = 4$ atom core of **1** possesses $3N - 6 = 6$ vibrational degrees of freedom. To limit the number of force constants and to avoid any redundancy-induced correlations among them, the torsional out-of-plane bending motion was neglected. This omission is warranted on the basis that contributions of out-of-plane bending motion to the Ni−O and O−O stretching modes should be insignificant.[23] The remaining three symmetry-inequivalent internal coordinates are the Ni−O and O−O stretching and the Ni−O−O bending coordinates with the associated force constants k_{Ni-O}, k_{O-O}, and k_{Ni-O-O}, respectively. An additional force constant k_{UB} was required to account for the Urey−Bradley nonbonded interaction between the Ni and nonadjacent O atoms. The force field for **1** employed in this analysis thus comprised the five normal modes listed in Table 1.

As the frequency of the δ_s(Ni−O−O) bending mode of **1** is unknown, k_{Ni-O-O} and k_{UB} were kept fixed at reasonable values of 0.30 mdyn Å/rad^2 and 0.05 mdyn/Å, respectively. k_{Ni-O} and k_{O-O} were then optimized for best agreement between the computed and experimental frequencies, using initial estimates of 1.7 and 2.6 mdyn/Å, respectively. With the refined force constants for **1** of $k_{Ni-O} = 1.52$ mdyn/Å and $k_{O-O} = 2.58$ mdyn/Å, the calculated frequencies agree very well with the experimental values (Table 1). Notably, the frequency of 139 cm^{-1} predicted for the δ_s(Ni−O−O) mode is very close to the value of δ_s(Cu−O−O) = 140 cm^{-1} employed by Baldwin et al. in their NCA for **2**,[22] thus supporting our choice of k_{Ni-O-O}.

Table 1. Experimental and Calculated Vibrational Frequencies for **1**[a]

normal mode	sym	exptl freqs		normal coordinate analysis		
		$^{16}O_2$	$^{18}O_2$	$^{16}O_2$	$^{18}O_2$	force constants
ν(O−O)	a_g	778	735	779	735	$k_{O-O} = 2.58$
ν_s(Ni−O)	a_g	479	456	480	456	$k_{Ni-O} = 1.52$
ν_{as}(Ni−O)	b_u			459	439	
δ_s(Ni−O−O)	a_g			139	139	$k_{Ni-O-O} = 0.30\ (0.05)^b$
δ_{as}(Ni−O−O)	b_u			107	102	

[a] Calculated values were obtained from a normal coordinate analysis (NCA) of the Ni_2O_2 unit. Frequencies are given in cm^{-1}, and stretching and bending force constants k are given in mdyn/Å and mdynÅ/rad^2, respectively. [b] Urey−Bradley nonbonding interaction constant in mdyn/Å.

To facilitate comparison of the force constants for the M−O and O−O stretches in trans end-on peroxo-bridged $(Ni^{2+})_2$ and $(Cu^{2+})_2$ dimers, we also performed a NCA on **2**, using the same force field and values for k_{M-O-O} and k_{UB} as for **1** along with the structural parameters and vibrational frequencies reported for **2**.[22] Significantly, the values of both $k_{Cu-O} = 2.05$ mdyn/Å and $k_{O-O} = 3.09$ mdyn/Å obtained for **2** are considerably larger than $k_{Ni-O} = 1.52$ mdyn/Å and $k_{O-O} = 2.58$ mdyn/Å determined for **1** (Table 3; detailed results for **2** are listed in Tables S10 and S11). Thus, the M−O and O−O force constants are 26% and 16%, respectively, lower in **1** than in **2**. The electronic origin of this difference will be explored in the Discussion.

In end-on peroxo-bridged dimers, the kinematic coupling between the M−O and O−O stretches is a sensitive function of the M−O−O bond angle γ.[23] This coupling becomes larger as γ grows and leads to an increase in the energetic separation between the ν_s(M−O) and ν(O−O) modes relative to the uncoupled system. To assess the effect of mechanical coupling between the Ni−O and O−O modes on the vibrational frequencies of **1**, an additional NCA was performed for a hypothetical model (**1-107**°) derived from **1** by reducing γ to 107.7° as in **2** and using the force constants determined for **1** (i.e., with $\gamma = 120°$). As shown in Table 3, the frequency of ν_s(Ni−^{16}O) is considerably higher in **1-107**° (505 cm^{-1}) than in **1** (479 cm^{-1}), while ν(^{16}O−^{16}O) is reduced from 778 cm^{-1} to 759 cm^{-1}. This result reflects the expected decrease in kinematic coupling between the M−O and O−O stretches with decreasing M−O−O angle γ and indicates that the relatively low value of ν_s(Ni−O) = 479 cm^{-1} in **1** compared to ν_s(Cu−O) = 561 cm^{-1} in **2** is due primarily to electronic rather than geometric factors. Conversely, the increased kinematic coupling in **1** compared to **2** partially offsets the decrease of ν(O−O) caused by electronic factors (Table 3). This difference in mechanical coupling between **1** and **2** is particularly evident from the potential energy distributions (PEDs; see Tables 2 and S11, respectively), which reveal that the contribution of M−O

Table 2. Normal Mode Descriptions for the $Ni_2(^{16}O)_2$ Unit

		eigenvectors[a]			PED[b]			
normal mode	sym	O−O	Ni−O	Ni−O−O	O−O	Ni−O	Ni−O−O	UB[c]
ν(O−O)	a_g	+0.349	−0.116	−0.036	87.9	11.4	0.2	0.5
ν_s(Ni−O)	a_g	+0.055	+0.159	−0.284	5.7	56.6	35.7	2.0
ν_{as}(Ni−O)	b_u	0.000	±0.199	±0.001	0.0	97.4	0.0	2.6
δ_s(Ni−O−O)	a_g	+0.014	+0.033	+0.099	4.3	29.7	51.2	14.8
δ_{as}(Ni−O−O)	b_u	0.000	±0.002	∓0.099	0.0	0.3	87.0	12.7

[a] Mass-weighted eigenvectors $\mathbf{L}_n$. [b] Potential energy distribution (PED) in %. [c] Urey−Bradley nonbonded interaction.

Table 3. Comparison of Stretch Frequencies (in cm^{-1}) and Force Constants (in mdyn/Å) for the $M_2(^{16}O)_2$ Units in **1**, **1-107°**, and **2**

model	ν_s(O−O)	k_{O-O}	ν_s(M−O)	k_{M-O}
1	778	2.58	479	1.52
1-107°	759	2.58	505	1.52
2	832	3.09	561	2.05

motion to the ν(O−O) normal mode is quite substantial for **1** but rather insignificant for **2**. This difference may also be responsible for the fact that, in rR spectra of **1**, ν(O−O) is more strongly enhanced relative to ν_s(M−O) than in rR spectra of **2**.[22]

2. Nature of Ni−O and O−O Bonding. A main objective of this study was to develop a quantitative bonding description for **1** so as to establish a suitable basis for a quantitative comparison between Ni−peroxo and Cu−peroxo bonding. The geometry and wave functions obtained from the BS (M_S = 0) DFT calculation on **1** will be used in all subsequent analyses because this state, which is computed 0.027 eV lower in energy than the corresponding HS state (Table S9), provides a better description of the exchange-coupled dimer ground state of **1**.

Our DFT computation for the BS state reveals that the two unpaired electrons on each Ni center occupy the Ni z^2- and x^2-y^2-based orbitals that are involved in Ni−O and Ni−N σ bonding, respectively.[46] Due to spin polarization, the majority-spin orbitals (β for Ni1, α for Ni2) are strongly stabilized relative to their unoccupied minority-spin counterparts. Because in the BS approach the spin-up (α) and spin-down (β) electrons are allowed to localize on opposite sides of the dimer, each spin-up MO has a C_2-symmetric spin-down counterpart that possesses the same energy and composition. This fact allows us to develop Ni−O and O−O bonding descriptions for **1** by considering solely the Ni1 3d- and O π*-based spin-up MOs, whose energies and compositions are listed in Table 4.

The dominant Ni−O bonding interaction can be inferred from the σ-antibonding MO Ni1(z^2),α and its bonding counterpart $O_2(\pi^*_\sigma)$,α shown in Figure 5. Both MOs possess substantial contributions from the Ni1 z^2 and peroxo π^*_σ parent orbitals, indicating that the Ni−O bonds are quite covalent. Due to its Ni−O σ-bonding nature, the peroxo π^*_σ-based MO, $O_2(\pi^*_\sigma)$,α, is strongly stabilized relative to the peroxo π^*_v-derived MO, $O_2(\pi^*_v)$,α (Table 4), the latter of which is essentially Ni−O nonbonding because its orientation perpendicular to the Ni_2O_2 plane precludes significant orbital overlap with the Ni 3d orbitals (Figure 5). The

Table 4. Energies (in eV) and Compositions of the Spin-Up Ni1 3d- and Peroxo-Based Molecular Orbitals Obtained from a B3LYP DFT Calculation on the BS (M_S = 0) State of **1**[a]

			left			right		
MO[b]	E (eV)	occ	N	Ni1	O1	O2	Ni2	N
Ni1(x^2-y^2),α	−5.508	0	8	78	0	0	0	8
Ni1(z^2),α	−6.823	0	1	59	16	4	0	0
$O_2(\pi^*_v)$,α	−9.435	1	1	4	46	42	2	0
$O_2(\pi^*_\sigma)$,α	−10.215	1	1	19	40	26	5	0
Ni1(yz),α	−11.971	1	4	73	3	4	3	6
Ni1(xz),α	−11.990	1	5	65	1	10	4	5
Ni1(xy),α	−12.295	1	0	95	0	0	0	0

[a] Only Ni 3d and O, N 2p orbital contributions are shown. [b] MOs are labeled according to the atomic orbitals that produce the dominant contribution.[46]

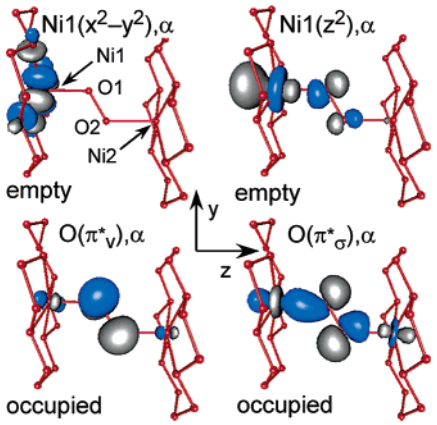

Figure 5. Isosurface plots of key spin-up MOs (isodensity value of 0.05 au) obtained from a spin-unrestricted B3LYP DFT computation on the BS (M_S = 0) state of **1**.

dominant Ni−N σ-bonding interaction on each monomer half involves the Ni x^2-y^2 orbital and the N p_x,p_y-based lone pairs of the macrocycle, which is evident from the σ-antibonding Ni1(x^2-y^2),α MO (Table 4). The fact that contributions from the N p_x,p_y-based lone pairs of the tmc macrocycle to this MO are relatively small indicates that the Ni−N bonds are considerably less covalent than the Ni−O bonds.

3. Exchange Coupling. The two high-spin (S = 1) Ni centers in **1** are expected to be antiferromagnetically coupled on the basis of qualitative considerations,[47] yet this coupling must be sufficiently weak to allow for the observation of paramagnetically shifted ^{1}H NMR resonances at 228 K.[15] Although the thermal instability of **1** prevented a reliable experimental determination of the exchange splitting, we can

(46) Throughout the manuscript, Ni 3d orbitals are labeled using an abbreviated notation (e.g., *xy* stands for d_{xy}).

(47) Bencini, A.; Gatteschi, D. *Electron Paramagnetic Resonance of Exchange Coupled Systems*; Springer-Verlag: Heidelberg, Germany, 1990.

estimate the magnitude of the exchange parameter J from our DFT computations. Using the Heisenberg−Dirac−van Vleck operator $H = -2J\mathbf{S}_1\cdot\mathbf{S}_2$ together with the formalism developed by Noodleman and co-workers,[48] J can be expressed in terms of the calculated total energies of the HS[49] and BS states (E_{HS} and E_{BS}, respectively) and $S_{max}^2 = 4$; i.e., $J = (E_{BS} - E_{HS})/S_{max}^2 = -170$ cm^{-1}. Note that this computed J value should be considered as an upper limit, as the DFT method typically overestimates covalency and hence antiferromagnetic exchange interactions.

The effectiveness of the Ni 3d-based MOs as superexchange pathways is governed by the extent of orbital contributions from the peroxide bridge and the second Ni center. A particularly clear representation of the antiferromagnetic exchange pathways is provided by the singly occupied natural MOs. In **1**, a single efficient pathway exists, involving the Ni z^2 and peroxo π^*_σ orbitals (Figure 4b). Interestingly, the estimated J value of -170 cm^{-1} for **1** is at least 3.5 times smaller than the value of $J = -600$ cm^{-1} determined experimentally for **2**.[22] To explore the possible source of this difference, it is useful to express the J value in terms of a sum of individual orbital contributions:[50]

$$J = \frac{1}{n_A n_B}\sum_{i,j} J_{A_i B_j} \qquad (1)$$

Here n_A and n_B denote the total numbers of unpaired electrons on the two metal centers A and B and $i, j = 1-5$ are their respective 3d orbitals. While in both **1** and **2** a single efficient antiferromagnetic superexchange pathway exists (vide supra),[22] its contribution to the total ground state J value is scaled by a factor of 1/4 in **1** ($n_A = n_B = 2$) relative to **2** ($n_A = n_B = 1$). Moreover, because of the considerably reduced covalency of the metal−peroxo bonds in **1** compared to **2** (see Discussion), the efficiency of this superexchange pathway will be significantly lower in the $(Ni^{2+})_2$ dimer than in the $(Cu^{2+})_2$ dimer.

D. Excited States. 1. TD-DFT Calculations and Spectral Assignments. The absorption spectrum of **1** exhibits a single intense band centered at 21 880 cm^{-1} that is assigned to a peroxo → Ni CT transition on the basis of the rR excitation profile data (Figure 1). To obtain quantitative insight into the excited-state structure of **1**, TD-DFT computations were performed for both the BS and HS states (in each case using the geometry-optimized model obtained for the BS state). As for both states the computed energies and intensities of the dominant transitions and the corresponding donor/acceptor MOs are similar, only the results from the BS calculation are used in the following analysis.

To allow for a visual comparison with the experimental data, the TD-DFT computed transition energies and intensities were used to simulate an absorption spectrum (Figure 6), assuming that each transition gives rise to a Gaussian band with a uniform width of 4700 cm^{-1}, corresponding to the experimentally determined width of the 21 880 cm^{-1} absorption feature. As a further means to facilitate this comparison, the calculated spectrum in Figure 6 was blue-shifted by 1600 cm^{-1} and the experimental intensities were scaled by a factor of 2.8. With these relatively minor adjustments, the overall agreement between the experimental and computed spectra is quite remarkable. Both spectra exhibit a single intense band below 33 000 cm^{-1} and the onset to a very intense absorption feature with a maximum above 33 000 cm^{-1}. On the basis of this comparison, it may be concluded that the TD-DFT method yields a reasonable description of the excited-state electronic structure of **1** and thus provides an excellent tool for assigning the major features observed in the experimental absorption spectrum.

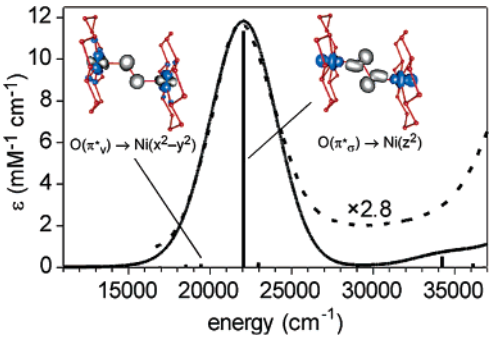

Figure 6. Theoretical absorption spectrum of **1** (thick solid line) obtained from B3LYP TD-DFT calculations on the BS ($M_S = 0$) state along with the corresponding experimental spectrum (dotted line). Individual transitions contributing to the computed absorption envelope are shown as vertical lines. To facilitate comparison with the experimental data, the calculated spectrum was blue-shifted by 1600 cm^{-1}, and the experimental intensities were scaled by a factor of 2.8. Electron density difference maps (EDDMs, isodensity value of 0.005 au) indicate loss (gray) and gain (blue) of electron density.

Analysis of the TD-DFT results reveals that the dominant transition in the visible region primarily involves peroxo π^*_σ → Ni z^2 CT excitation (i.e., promotion of an electron from the Ni−O σ-bonding MO to its σ-antibonding counterpart), which is particularly evident from the corresponding electron density difference map (EDDM) shown in Figure 6. Note that within the framework of the BS formalism, this peroxo → Ni CT transition can be regarded as involving transfer of half an electron from $O_2(\pi^*_\sigma),\alpha$ to $Ni1(z^2),\alpha$ and half an electron from $O_2(\pi^*_\sigma),\beta$ to $Ni2(z^2),\beta$.

A second CT transition is computed at 17 843 cm^{-1}; however, as this transition is 2 orders of magnitude less intense than the one predicted at 20 454 cm^{-1}, it does not contribute notably to the calculated absorption envelope. This second transition predominantly involves peroxo π^*_v → Ni x^2-y^2 CT excitation, carrying only little absorption intensity because of the lack of any peroxo π^*_v orbital character in the corresponding acceptor MO. These TD-DFT results are thus fully consistent with the experimental absorption spectrum that also exhibits a single intense feature in the visible region (Figure 6).

2. Peroxo-to-Nickel Charge Donation. The energy and integrated intensity of the dominant peroxo π^*_σ → Ni z^2 CT

(48) Noodleman, L. *J. Chem. Phys.* **1981**, *74*, 5737.
(49) Note that for the determination of the J value, the energy of the HS state (E_{HS}) was calculated using the geometry-optimized model for the BS state, as the Heisenberg−Dirac−Van Vleck operator is only applicable if the geometry of the cluster remains constant in all dimer spin states.
(50) Ferguson, J.; Guggenheim, H. J.; Tanabe, Y. *J. Phys. Soc. Jpn.* **1966**, *21*, 692−704.

transition at 21 880 cm^{-1} in the absorption spectrum of **1** (Figure 1) can be used to estimate the total amount of Ni 3d orbital character in the peroxo π^*_σ-based MO, which provides an experimental measure of the σ-donor strength of the peroxo group in this dimer. As the Ni−O bonding interactions in **1** exclusively involve the peroxo π^*_σ and Ni z^2 orbitals (section D.1), the contribution from the half-occupied Ni z^2 orbitals to the peroxo π^*_σ orbital is approximately given by eq 2 that relates the charge donation of the peroxo ligand to the intensity of the peroxo → Ni CT transition:[51]

$$(C^{d}_{\pi^*})^2 = \kappa \frac{f}{\nu |\mathbf{r}|^2} \qquad (2)$$

$\kappa = 9.22 \times 10^{-2}$ Å is a constant, f and ν are the oscillator strength and transition energy of the peroxo π^*_σ → Ni z^2 CT transition, respectively, and **r** is the transition vector that coincides with the Ni−O bond vector. While $(C^{d}_{\pi^*})^2$ does not provide an absolute measure of covalency, it serves as a useful reference for a comparison with other end-on peroxo-bridged dimers (see Discussion). Using the experimental values $f = 0.0912$[52] and $\nu = 21\ 880\ cm^{-1}$, along with the DFT-optimized Ni−O bond length of $|\mathbf{r}| = 2.015$ Å (section B), a value of $(C^{d}_{\pi^*})^2 = 0.94$ is obtained relative to that reported for an end-on peroxo Cu^{2+} monomer, which is the reference value typically used.[51]

3. Excited-State Distortions. It is interesting to note that, upon peroxo → Ni CT excitation of **1**, the O−O stretching mode at 778 cm^{-1} is considerably more strongly resonance-enhanced than the Ni−O stretch at 479 cm^{-1} (Figure 2). To explore the origin of this striking observation, we performed an excited-state distortion analysis of our experimental rR data. Excited-state distortions can be expressed in terms of changes in internal coordinates using the eigenvectors obtained from the NCA (Table 2) and the fitted dimensionless displacements $|\Delta_{778}| = 2.45$ and $|\Delta_{479}| = 0.5$ from the quantitative rR analysis (section A). Specifically, changes in internal coordinates Δr_i (Å) are related to displacements Δ_n along the normal coordinates n by[53]

$$\Delta r_i = 5.8065 \sum_n \frac{L_{i,n}\Delta_n}{\sqrt{\nu_n}} \qquad (3)$$

where $L_{i,n}$ is the ith element of the mass-weighted eigenvector $\mathbf{L}_n$ for the nth normal mode (Table 2). While the signs of the displacements cannot be determined experimentally, they can be inferred on the basis of the following considerations. Upon peroxo → Ni CT excitation, electron density is transferred primarily from the Ni−O σ-bonding MO to its antibonding counterpart (Figure 5), leading to a substantial weakening, and hence an elongation, of the Ni−O bonds; thus, we may conclude that $\Delta_{479} > 0$. On the other hand, while both the donor and acceptor MOs involved in this transition are O−O π-antibonding, the former contains considerably more peroxo π^* character than the latter (Figure 5, Table 4); consequently, the O−O bond is strengthened, and hence shortened, in the excited state, suggesting that $\Delta_{778} < 0$.

Using eq 3 and the fitted values $\Delta_{479} = +0.5$ and $\Delta_{778} = -2.45$ (section A), nuclear distortions of $\Delta r(\text{Ni−O}) = +0.08$ Å and $\Delta r(\text{O−O}) = -0.17$ Å are obtained. Therefore, the very weak rR enhancement of the Ni−O compared to the O−O stretch (Figure 2) does not actually reflect a correspondingly small distortion along the Ni−O bond vector upon peroxo → Ni CT excitation but, instead, arises from the strong coupling of the Ni−O and O−O stretching motions (Table 2).

Discussion

Comparison of Ni−Peroxo and Cu−Peroxo Bonding. The Ni−peroxo bonding description developed here for the trans-μ-1,2-peroxo-bridged $[\{(tmc)Ni^{2+}\}_2(O_2)]^{2+}$ dimer **1** can now be compared to the Cu−peroxo bonding description reported by Baldwin et al. for the trans-μ-1,2-peroxo-bridged $[\{(TMPA)Cu^{2+}\}_2(O_2)]^{2+}$ dimer **2**.[22] In both dimers, metal−peroxo bonding is dominated by σ interactions between the metal z^2 orbitals and the peroxo π^*_σ orbital.[54] The additional hole per Ni^{2+} (d^8) relative to Cu^{2+} (d^9) occupies the Ni x^2-y^2-based MO that is oriented perpendicular to the Ni−O bond vector and, therefore, does not participate in Ni−O bonding. However, despite the similar nature of metal−peroxo bonding in **1** and **2,** the M−O and O−O stretch force constants, and thus the corresponding bond strengths, are 26% and 16%, respectively, lower in the $(Ni^{2+})_2$ dimer (Table 3). This difference in metal−peroxo bond strength is also apparent from the substantially longer M−O distances in **1** (2.015 Å) than in **2** (1.852 Å). These results can be rationalized by noting that the peroxo → metal σ-donation leads to a decrease in electron density in the peroxo π^*_σ orbital that is π antibonding with respect to the O−O bond. Thus, an increase in metal−peroxo bond strength will simultaneously also lead to a stronger O−O bond. On the basis of simple bonding considerations,[55] three principal factors are expected to determine the strength of the M−O σ-interaction in end-on peroxo dimers: (i) the energy splitting between metal 3d and peroxo π^* orbitals; (ii) the donor strength of the supporting ligands; (iii) the M−O−O angle γ. The relative importance of these three factors with respect to the differences in Ni−peroxo and Cu−peroxo bonding in **1** and **2** is evaluated next.

First, the covalency, and thus the strength, of the metal−peroxo bonds is influenced by the relative energies of the metal 3d and peroxo π^* orbitals. Because of the lower

(51) Baldwin, M. J.; Root, D. E.; Pate, J. E.; Fujisawa, K.; Kitajima, N.; Solomon, E. I. *J. Am. Chem. Soc.* **1992**, *114*, 10421−10431.

(52) This value was obtained from $f = 4.62 \times 10^{-9}$ M $cm^2 \cdot \epsilon \cdot \Delta\nu$, where $\epsilon = 4200\ M^{-1}\ cm^{-1}$ and $\Delta\nu = 4700\ cm^{-1}$.

(53) Myers, A. B.; Mathies, R. A. In *Biological Applications of Raman Spectroscopy*; Spiro, T. G., Ed.; Wiley: New York, 1987; Vol. 2, pp 1−58.

(54) In **2**, a weak Cu−peroxo π interaction leads to significant intensity of the peroxo π^*_v → Cu z^2 CT transition through mixing of the z^2 orbital with other Cu 3d orbitals.[22] However, as these other orbitals are doubly occupied, this π interaction does not provide a net contribution to Cu−O bonding.

(55) Ballhausen, C. J. *Introduction to Ligand Field Theory*; McGraw-Hill: New York and London, 1962.

effective nuclear charge of Ni^{2+} ($Z_{eff} = 7.20$) compared to Cu^{2+} ($Z_{eff} = 7.85$),[56] the Ni^{2+} 3d orbitals are higher in energy than the Cu^{2+} 3d orbitals. Consequently, the metal−peroxo bonding interaction will be considerably weaker in **1** than in **2**. Second, increasing the donor strength of the supporting ligands decreases electron donation from the peroxo π^*_σ orbital to the metal and, hence, the metal−peroxo bonding interaction. Although the combined donor strength of the amine nitrogens of the tmc ligand in **1** is expected to be slightly larger than that of the pyridine groups of the TMPA ligand in **2** (also note that π-back-bonding in the latter complex might slightly lower the energies of the Cu^{2+} 3d orbitals), this difference should have only a minor influence on the metal−peroxo bond strength. In support of this assumption, a recent study by Solomon and co-workers revealed that, upon substitution of protons on the TMPA ligand in **2** by electron-donating Me_2N groups, both the Cu−O and O−O stretch frequencies decrease only slightly, corresponding to reductions in the respective force constants by a mere 3%.[57,58] Finally, with increasing M−O−O angle γ the overlap of the metal z^2 and peroxo π^*_σ orbitals decreases, thus weakening the metal−peroxo bond. However, according to the angular overlap model this orbital overlap is proportional to sin γ,[59] suggesting that it is only ∼9% lower in **1** ($\gamma = 120°$) than in **2** ($\gamma = 107.7°$).

Collectively, these results suggest that the lower effective nuclear charge of Ni^{2+} relative to Cu^{2+} is the major cause of the drastically reduced metal−peroxo bond covalency and, thus, the decreased M−O and O−O bond strengths in **1** compared to **2**. A direct measure of the extent of metal−peroxo bond covalency is provided by the amount of peroxo → metal charge donation $(C^d_{\pi^*})^2$ that can be estimated from the energy and intensity of the dominant peroxo → metal CT transition.[51] For **1**, a value of $(C^d_{\pi^*})^2 = 0.94$ was determined (section D.2), which amounts to only half of the value reported for **2**, $(C^d_{\pi^*})^2 = 1.9$ (both values are given relative to that reported for an end-on peroxo Cu^{2+} monomer).[51] This ∼50% difference in metal−peroxo bond covalency between **1** and **2** concurs nicely with the drastically weaker M−O and O−O bonds in the former.

Our results indicate that the larger metal−O−O angle in **1** than in **2** is caused by steric rather than electronic effects. Specifically, upon replacement of the tmc macrocycle of **1** by sterically nondemanding ammines (model **1′**), the DFT-optimized Ni−O−O angle decreases from $\gamma = 120°$ to 108.7°, thus closely approaching the Cu−O−O angle of $\gamma = 107.7°$ observed in the X-ray structure of **2**. Moreover, this value of $\gamma = 108.7°$ obtained for **1′** is in fact somewhat smaller than the average Co−O−O angle of $\gamma = 112°$ displayed by a series of 22 structurally characterized end-on peroxo-bridged $(Co^{3+})_2$ dimers.[60] As in all of these dimers π-contributions to metal−peroxo bonding are negligible, the M−O−O angle is expected to be tuned such as to maximize the metal z^2−peroxo π^*_σ σ-bonding interaction; thus, in the absence of steric strain, a value of $\gamma \approx 110°$ appears most favorable. Note that the situation for **1** is fundamentally different from that encountered for cis end-on peroxo-bridged $(Fe^{3+})_2$ dimers, despite the fact that the latter possess similarly large metal−O−O bonding angles ($\gamma = 120-129°$). For $(Fe^{3+})_2$ species, the tendency to adopt large values of γ reflects the presence of additional Fe−O π-bonding interactions,[23] while the large γ value for **1** is due primarily to the steric constraints imposed by the tmc supporting ligands.

End-On → Side-On Peroxo Ni_2O_2 Core Conversion. As described previously,[15] **1** is thermally unstable and decomposes via a brown intermediate to a stable $[(tmc)Ni^{2+}OH]^+$ species.[16] Although the brown intermediate is relatively long-lived at low temperature ($\tau_{1/2} \approx 4$ h at −40 °C), its structural and electronic properties have yet to be defined. A feasible mechanistic pathway for the decomposition of **1** would involve initial conversion to the corresponding side-on peroxo dimer concomitant with tmc ligand folding, followed by O−O bond scission to afford the bis-μ-oxo $(Ni^{3+})_2$ isomer and, last, H-atom abstraction from the hydrocarbon solvent to yield the final product $[(tmc)Ni^{2+}OH]^+$ (Scheme 1).

To assess the likelihood of such a decay pathway involving transient formation of a μ-η^2:η^2 side-on peroxo-bridged $(Ni^{2+})_2$ isomer of **1**, a series of DFT computations were performed. First, a simplified model of the hypothetical μ-η^2:η^2-peroxo $(Ni^{2+})_2$ dimer possessing ammine ligands (**3′**) was generated using symmetry-unrestricted DFT geometry optimizations for both the HS ($S = 2$) and BS ($M_S = 0$) states. The resulting O−O bond lengths of 1.474 and 1.484 Å, respectively, are typical for a bridging peroxo moiety (key structural and electronic parameters for **3′** are listed in Table S9). For the BS state this side-on peroxo dimer model **3′** was found to be stabilized by 0.20 eV (4.8 kcal/mol) relative to its end-on counterpart **1′**, while for the HS state it is slightly destabilized by 0.04 eV (0.9 kcal/ mol; see Table S9). Thus, in the presence of sterically nondemanding ligands on the two monomer halves, the side-on and end-on peroxo $(Ni^{2+})_2$ core structures are essentially isoenergetic. This result suggests that the relative stabilities of the trans-μ-1,2-peroxo complex **1** and the corresponding μ-η^2:η^2-peroxo $(Ni^{2+})_2$ derivative are controlled by steric rather than electronic effects.

To explore the reaction coordinate and energy barrier for the interconversion between the end-on (**1′**) and side-on (**3′**) peroxo $(Ni^{2+})_2$ core structures, the Ni···Ni distance was reduced in fixed increments of 0.1 Å from 4.675 to 3.875 Å, and for each configuration a full DFT geometry optimization was performed with respect to all other degrees of freedom except for the dihedral angle τ, which was kept at 0° to ensure a smooth core conversion. Importantly, the

(56) Slater, J. C. *Quantum Theory of Atomic Structure*; McGraw-Hill: York, PA, 1960; Vol. 1, p 112.
(57) Henson, M. J.; Vance, M. A.; Zhang, C. X.; Liang, H.-C.; Karlin, K. D.; Solomon, E. I. *J. Am. Chem. Soc.* **2003**, *125*, 5186−5192.
(58) This comparison is based on the assumption that the kinematic coupling between the normal modes remains constant, which is justified by the fact that steric interactions are hardly altered upon ligand substitution.
(59) (a) Schäffer, C. E. *Struct. Bonding* **1968**, *5*, 68. (b) Weihe, H.; Güdel, H. U. *J. Am. Chem. Soc.* **1998**, *120*, 2870−2879.
(60) (a) Niederhoffer, E. C.; Timmons, J. H.; Martell, A. E. *Chem. Rev.* **1984**, *84*, 137−203. (b) Barraclough, C. G.; Lawrance, G. A.; Lay, P. A. *Inorg. Chem.* **1978**, *17*, 3317−3322. (c) Kayatani, T.; Hayashi, Y.; Suzuki, M.; Uehara, A. *Bull. Chem. Soc. Jpn.* **1994**, *67*, 2980.

computed potential energy curves for both the HS and BS states (Figure S1) exhibit no significant energy barrier for this end-on → side-on core conversion (note that by keeping τ fixed at 0°, both the HS and BS calculations suggest that the side-on isomer is slightly stabilized by ~0.25 eV (5.8 kcal/mol) relative to the end-on species). Additional computations for the HS state revealed that a further decrease in Ni···Ni distance to generate the bis-μ-oxo $(Ni^{3+})_2$ derivative of **1** leads to a decrease in total energy by ~5 kcal/mol, consistent with our previous finding[13] that in the presence of sterically nondemanding supporting ligands the bis-μ-oxo $(Ni^{3+})_2$ core structure is energetically favored over its peroxo $(Ni^{2+})_2$ alternatives.

To assess the role of steric factors in controlling the relative stabilities of end-on and side-on peroxo $(Ni^{2+})_2$ core structures, DFT computations were also performed on a hypothetical side-on peroxo dimer model of $[\{(tmc)Ni\}_2O_2]^{2+}$ equipped with the complete tmc ligand.[61] A "folded" tmc conformation was chosen so as to allow for two cis-oriented oxygen-binding sites at each Ni center (model **3***; key geometric parameters are summarized in Table S7). The large size of this model required that DFT computations be performed by imposing C_2 symmetry on the dimer structure and wave functions, thereby restricting our analysis to the HS state. Significantly, during geometry optimization the side-on peroxo starting model **3*** converted spontaneously to an end-on bridged species (model **1a***) that is stabilized by 2.94 eV (68 kcal/mol) relative to **3***. Notably, model **1a*** still possesses the folded tmc conformation, indicating that a significant energy barrier exists for ligand unfolding. To estimate the energy for the complete end-on → side-on peroxo Ni_2O_2 core conversion, an additional geometry optimization was performed on a full model of **1** with the tmc macrocyle in the unfolded conformation (model **1***); it was found that **1*** is stabilized by 0.75 eV (17.3 kcal/mol) relative to its conformational isomer **1a***.

Collectively, our computational data suggest that the conversion of **1** to a μ-η^2:η^2-peroxo-bridged $(Ni^{2+})_2$ species is energetically unfavorable by ~85 kcal/ mol (estimated from the difference in calculated total energies for models **3*** and **1***), as the small electronic driving force associated with the end-on → side-on peroxo core conversion is insufficient to overcome the steric constraints imposed by the tmc supporting ligands. Therefore, a reaction pathway for the thermal decay of **1** involving initial conversion to the corresponding side-on peroxo $(Ni^{2+})_2$ isomer (as outlined in Scheme 1) can be ruled out on the basis of our computations.

Summary and Conclusions

Together, the spectroscopic and computational studies on the μ-1,2-peroxo-bridged $(Ni^{2+})_2$ dimer $[\{(tmc)Ni^{2+}\}_2(O_2)]^{2+}$ (**1**) reported here provide quantitative insight into the geometric and electronic properties of the Ni_2O_2 core in this species. Both the Ni−O and O−O bonds in **1** are substantially weaker than the Cu−O and O−O bonds in the trans-μ-1,2-peroxo-bridged $(Cu^{2+})_2$ complex $[\{(TMPA)Cu^{2+}\}_2(O_2)]^{2+}$ (**2**) due primarily to the decreased effective nuclear charge of Ni^{2+} compared to Cu^{2+} and the consequent drastic reduction in covalency of the metal−peroxo bonds. This reduced covalency is expected to lead to a substantially increased negative charge density on the peroxo moiety in **1** relative to **2**, suggesting that, in general, μ-1,2-peroxo-bridged $(Ni^{2+})_2$ dimers should display a higher potency for hydrogen abstraction than their $(Cu^{2+})_2$ analogues. This increased reactivity of μ-1,2-peroxo-bridged $(Ni^{2+})_2$ dimers may suggest that the thermal decay of **1** to the final product $[(tmc)Ni^{2+}OH]OTf$ begins with H-atom abstraction from the CH_3CN solvent by the bridging peroxide moiety. Alternatively, a decay mechanism invoking initial conversion of **1** to a μ-η^2:η^2-peroxo-bridged $[\{(tmc)Ni^{2+}\}_2(O_2)]^{2+}$ intermediate is not supported by our computations, as this species is predicted to be destabilized by ~85 kcal/mol relative to **1** due to the steric constraints imposed by the tmc ligands.

Acknowledgment. T.C.B. thanks the University of Wisconsin−Madison and the Sloan Research Foundation Fellowship Program for generous support. C.G.R. acknowledges generous financial support by the NSF (Grant CHE-0213260).

Supporting Information Available: Atomic coordinates of the geometry-optimized models **1**, **1′**, **3′**, **1***, and **3*** (Tables S1−S8), key bond lengths and angles, unpaired spin densities, and total energies for **1**, **1′**, **3′**, **1***, and **3*** (Table S9), an NCA analysis for **2** (Tables S10 and S11), and potential energy curves associated with the end-on → side-on peroxo $(Ni^{2+})_2$ core conversion (Figure S1). This material is available free of charge via the Internet at http://pubs.acs.org.

IC048584J

(61) The role of steric factors in controlling the relative stabilities of related side-on and end-on peroxo $(Cu^{2+})_2$ dimers has been evaluated previously by Bérces within the framework of DFT computations: Bérces, A. *Inorg. Chem.* **1997**, *36*, 4831−4837.